Transport properties of saline CO_2 storage reservoirs with unconnected fractures from brine-CO_2 flow-through tests

by

Andrea Muñoz-Ibáñez[a*]

Ismael Himar Falcon-Suarez[b]

Héctor Marín-Moreno[b]

Jordi Delgado-Martín[a]

&

Peter Mackin[c]

[a]School of Civil Engineering, University of A Coruña, Campus de Elviña s/n, 15071 A Coruña, Spain

[b]National Oceanography Centre, University of Southampton Waterfront Campus. European Way, SO14 3ZH, Southampton, United Kingdom.

[c]University of Southampton, Ocean and Earth Science, Southampton, SO14 3ZH, UK

[*]Corresponding author: School of Civil Engineering, University of A Coruña, Campus de Elviña s/n, 15071 A Coruña, Spain.

Phone: +34-981-167000 Office: 5415 e_mail: andrea.munoz@udc.es

Abstract

CO_2 storage in fractured reservoirs may lead to fast CO_2 flow through interconnected fracture networks; but the role of isolated fractures on brine-CO_2 multiphase flow systems remains unclear. We present the results of a brine-CO_2 flow-through experiment in which we assess the change in transport properties of a synthetic sandstone plug (a surrogate of a saline siliciclastic CO_2 reservoir) containing non-connected fractures aligned 45º from its axis. The test was performed at 40 MPa of constant hydrostatic confining pressure and ~11 MPa of pore pressure, at room temperature (~19.5ºC), using pure liquid-CO_2 and 35 g L^{-1} NaCl salt solution. The injected CO_2-brine volume fraction was increased from 0 to 1 in 0.2 units-steps (drainage). Upon achievement of the maximum CO_2 saturation (S_{CO_2} ~0.6), the plug was flushed-back with the original brine (imbibition). During the test, we monitored simultaneously pore pressure, temperature, axial and radial strains, and bulk electrical resistivity. The fractured sample showed lower values of cross- and end-points in the relative permeability curves to CO_2 compared to non-fractured samples, from comparable experiments performed at similar pressure and brine salinity conditions, but different temperature. Our results suggest that a non-connected fracture network affects the mobility of the individual phases, favouring the trapping of CO_2 in the porous medium and improving the storage efficiency of the reservoir. These evidences show the need of a better understanding of fracture connectivity prior to discard fractured reservoirs as unsuitable geological formations for CO_2 storage.

Keywords: CO_2 geosequestration; fractures; hydromechanics; electrical resistivity; relative permeability.

1. Introduction

The success of large-scale CO_2 geosequestration and long-term storage highly depends on the capacity of the reservoir to avoid potential CO_2 leakage to the surface along permeable underground pathways. Depleted oil and gas reservoirs, saline aquifers, and coal seams have been recognized as suitable formations for CO_2 storage (IPCC, 2005). Among them, saline aquifers are the most attracting sites due to its worldwide distribution, high potential storage capacity and low reactivity to CO_2 (Bachu, 2015; Michael et al., 2010).

Enhanced chemical reactivity induced by the introduction of a non-resident fluid into rocks can also lead to significant modifications of their porosity and permeability (e.g., Canal et al., 2013). Even in reservoirs with low potential reactivity to CO_2 (e.g., sandstone), CO_2-induced salt precipitation can significantly affect the injection efficiency in the CO_2 storage site, as observed in Ketzin (Baumann et al., 2014) or in the Tubåen Formation at the Snøhvit Field (Grude et al., 2014). However, changes in permeability caused by mineral dissolution/precipitation strongly depend on the specific location where these processes occur (i.e. at open pore spaces or in necks or throats; Canal et al. (2013); Stack et al. (2014)) in connection to the main flow paths.

Rock wettability in brine-CO_2 systems affects the efficiency of the CO_2 injection process, the flow and distribution of fluids within the pore space, and the trapping capacity during CO_2 storage (Al-Menhali and Krevor, 2014). The wetting phase (brine) occupies the smallest pores while the non-wetting phase (CO_2) remains in the largest cavities (Dullien, 1992). Then, residual CO_2 saturations are higher in strongly brine-wet sandstones; while in CO_2-brine mixed-wet systems certain parts of the pore surface are preferentially wetted by one of the both fluids, leading to a lower residual trapping (Al-Khdheeawi et al., 2017). A number of factors influence the wettability of

rock-fluid systems, such as pressure, temperature and brine salinity (Al-Khdheeawi et al., 2017). Water-wettability decreases (reciprocally, CO_2-wettability increases) with pressure and brine salinity, and increases with temperature in the presence of common sandstone minerals such as mica or quartz (Broseta et al., 2012; Chiquet et al., 2007).

Capillary pressure is a key factor impacting fluid transport in the formation and determines the ability of the wetting phase to prevent the non-wetting phase to flow through the sample. It increases with the interfacial tension (IFT), decreases with the pore radius (Chiquet et al., 2007), and also depends on wettability (e.g., Krevor et al., 2015; Wang and Tokunaga, 2015). According to Bachu and Bennion (2009), IFT increases with temperature and water salinity and decreases with pressure. Pore shape and connectivity also influence CO_2 displacement at the pore scale. The relative abundance of necks and throats in the overall rock framework constrains the capillary threshold to be exceeded to initiate CO_2 migration (Zhu et al., 2016). The heterogeneities in the pore space result in heterogeneous trapping of the non-wetting phase (Tsuji et al., 2016).

The study of fluid mobility is commonly addressed by flow-through experiments under reservoir conditions in the laboratory, typically complemented with non-intrusive techniques such as computed tomography (CT) scanning (Akbarabadi and Piri, 2013; Krevor et al., 2012), magnetic resonance imaging (Almenningen et al., 2018), or electrical resistivity (Carrigan et al., 2013; Falcon-Suarez et al., 2016; Nakatsuka et al., 2010). Electrical resistivity is also used as a remote sensing technique for monitoring the CO_2 plume advance in saline aquifers (i.e., controlled-source electromagnetic surveys – CSEM, e.g., Park et al. (2013)), due to the strong resistivity contrast between brine (low resistivity) and CO_2 (high resistivity). The degree of brine

saturation can be inferred from electrical resistivity using Archie's law (Archie, 1942). The application of Archie's law relies on the accurate resistivity estimate of the fully-saturated rock, the resistivity of pore fluid, and the shape properties of the electrically-connected porosity fraction (Cai et al., 2017). The resistivity-saturation conversion has been previously used to map CO_2 distribution in partially saturated porous media in a number of CO_2-brine flow-through tests (e.g., Alemu et al., 2013; Nakatsuka et al., 2010; Z. Wang et al., 2009), as an alternative to X-ray CT-scanning (e.g., Berg et al., 2013; Krevor et al., 2012).

To some extent, all CO_2 storage formations are fractured reservoirs (Iding and Ringrose, 2010). Therefore, fracture density and distribution, orientation and connectivity need to be precisely assessed to guarantee safe and long-term geological storage of CO_2 (Bond et al., 2013). Different models have been proposed to describe multiphase flow through an individual fracture (e.g. Huo and Benson (2016)), and validated from experimental studies on artificial samples with ideal smooth and parallel surfaces (Diomampo, 2001; Fourar and Bories, 1995). However, experimental studies on natural rock samples with a single fracture highlight the limitations of the proposed models when upscaling results to multiphase flow on real fractured reservoir formations (Noriaki et al., 2015).

Assessing the fracture connectivity effect on multiphase flow is challenging both in nature and laboratory scales. Interconnected fracture networks may act as path-flow in low permeability formations (Nooraiepour et al., 2018). In principle, the high hydraulic conductivity of the fractures would lead to preferential path-flows for CO_2, diminishing the storage effectivity in the rock matrix and hampering the CO_2 migration control (March et al., 2018). However, when a high density of non-connected fractures

exists in the reservoir, their effect on the hydrodynamic behaviour of CO_2 storage systems is unclear, and yet to be investigated.

In this contribution, we deepen into this aspect and present the results of a brine-CO_2 flow-through experiment performed on a synthetic sandstone sample containing well-distributed non-connected fractures aligned at 45º from its axis. We focus on assessing the transport properties of non-connected fractured saline siliciclastic CO_2 storage reservoirs, by analysing CO_2-induced changes in electrical resistivity and relative permeability. The experiment is complemented with (i) post-test thin section observations, (ii) reactive transport modelling, and (iii) comparison with previous experiments performed under similar conditions but using non-fractured synthetic sandstone samples.

2. Materials and methods

2.1. Synthetic sandstone

We used a 50 mm diameter 20 mm length silica-cemented synthetic sandstone plug, with spread aligned fractures oriented at 45º from its axis. The sample belongs to the same batch used by Tillotson et al. (2012), and later used by Amalokwu et al. (2015) to study water saturation and stress effects on shear wave splitting at oblique angles, using de-ionized water (DIW) as saturating fluid. Specific details concerning its preparation are given therein, but we explain here the main aspects for completeness. During the manufacturing process, aligned fractures were conformed in a paralepipedic block at the time of sample manufacturing by horizontally spreading 2 mm-diameter, 200 μm-thick penny-shape aluminium elements (Al-discs), in four layers with a vertical separation of ~4 mm. After the thermal (manufacturing) treatment, the block was cored ensuring an angle of 45º for the Al-disc layers. The resulting

sample was flushed with 10% HCl solution to etch the fractures by leaching the aluminium. The morphology of the sample was checked by X-ray CT scan imaging, from which a fracture density ε_f = 0.0289 ±0.0077 was determined (Tillotson et al., 2012). Since ε_f is related to the number of fractures N with radius a per unit volume V as $\varepsilon_f = N\, a^3\, V^{-1}$ (Mavko et al., 2009), we estimate the pore volume fraction of sample 45A corresponding to fractures is ~10%.

Before the brine-CO_2 flow-through (BCFT) test, porosity (ϕ_0) was measured by He-pycnometry and intrinsic permeability ($k_{gas,0}$) by N_2-permeameter under low confining pressure conditions (~0.5 MPa). Table 1 shows the main physical properties of the sample.

Table 1. Sample properties before test.

Sample	Length (mm)	Diameter (mm)	ϕ_0 ($m^3\ m^{-3}$)	$k_{gas,0}$ (mD)	$^*\rho_b$ ($kg\ m^{-3}$)
45A	19.85	49.54	0.273	5.48	1812

$^*\rho_b$ is the bulk density

2.2. Experimental setup

The experimental rig (Figure 1) is designed around a modified Hoek-Franklin type triaxial core holder (previously described in Falcon-Suarez et al., 2016), which allows the simulation of reservoir conditions up to 65 MPa of confining and pore pressure. This system is capable to measure electrical resistivity and axial and radial strains simultaneously, during the co-injection of up to two different pore fluids.

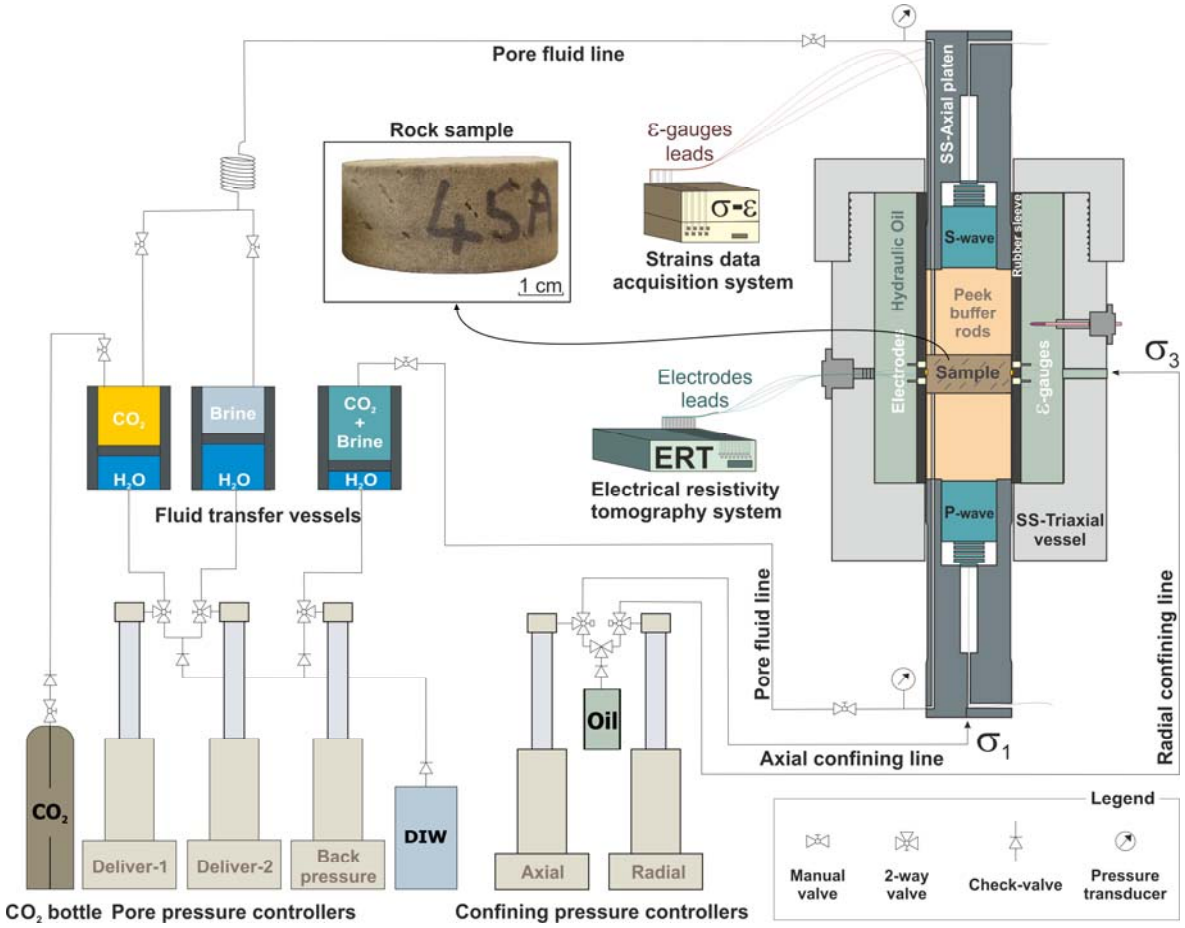

Figure 1. Experimental setup and synthetic sandstone with non-connected fractures aligned at 45º from its axis (sample 45A).

To track the axial and radial displacements occurring during the experiment, a rosette of two 350-ohm strain gages (90º configuration) was epoxy-glued onto the lateral surface of the sample. Inside the triaxial cell, a 6 mm thick, 190 mm height nitrile-hydrogenated butadiene rubber (NHBR) sleeve isolates the sample plug from the mineral oil used to deliver confining pressure. The sleeve is equipped with 16 stainless steel electrodes arranged in two rings around the plug that provide electrical resistivity measurements, once in contact with the sample. The system uses a tetra-polar electrode configuration to minimize electrode polarization artefacts. For any single operational run, the electrical resistivity tomography (ERT) system acquires 208 individual tetra-polar measurements using various permutations of current injection

and potential difference sensing electrode pairs. The whole acquisition lasts ~20 s. The gathered data are then inverted using software based upon EIDORS (Adler and Lionheart, 2006) MATLAB toolkit for a uniform/homogeneous isotropic resistivity and heterogeneous isotropic resistivity distribution. Both inversion schemes employ a finite element forward model of the sample and electrodes (further details in North et al., 2013). For this test, the system was configured to discard the measurements at the electrodes nearby the strain gauges, providing an accurate result for the bulk resistivity but hampering the tomography inversion. Under our experimental *P*-*T*- fluid salinity conditions and sample permeability, the associated resistivity error is ~1% (for frequencies between 1 and 500 Hz), for homogenous and isotropic rock samples in the electrical resistivity range 1 to 100 Ω m. Above this resistivity and for the case of non-isotropic materials, the error may rise up to 5% (North et al., 2013).

Axial stress is applied through two stainless-steel platens, which allow pore fluid circulation through the sample via thru-holes. The platens are specially designed to bypass the leads from the strain gauges glued to the sides of the plug, which are then connected to a 4-channel data acquisition system (Vishay-Model D4).

The experiment was conducted under hydrostatic confining stress condition ($\sigma_1 = \sigma_2 = \sigma_3$) automatically controlled with a dual ISCO EX-100D system. Upstream pore pressure was also controlled with an additional ISCO EX-100D system, configured to independently deliver brine and CO_2. A third ISCO ED100 pump was used as backpressure regulator downstream of the sample. In order to prevent the controller from potential damage due to direct contact with the corrosive brine and CO_2 solutions, the pore fluids are indirectly delivered/received using fluid transfer vessels (FTVs). For this experiment, two FTVs supplied pure liquid-CO_2 and 35 g L^{-1} NaCl salt solution, respectively, while a third one received the resulting fluid downstream. Additionally,

two piezo-resistive pressure transmitters (Keller model PA-33X) placed very close to the inlet (upstream) and outlet (downstream) ports allowed accurate control of the pore pressure.

2.3. Experimental procedure: Brine-CO_2 flow-through test

The test simulates a CO_2 injection scenario in a siliciclastic saline reservoir with non-connected aligned fractures. We performed a brine-CO_2 flow-through (BCFT) test using the steady-state technique (Dullien, 1992), with drainage (i.e., the progressive displacement of a resident saline fluid with CO_2) and imbibition (i.e., the back-displacement of CO_2 by saline fluid) episodes, similar to the experimental approach described in Falcon-Suarez et al. (2018, 2017, 2016).

Before starting the experiment, the plug was oven-dried at 60 ºC for 24 h and then saturated with a 35 g L^{-1} NaCl deairated aqueous solution (brine), representing the resident fluid in a potential reservoir. The dry sample was placed in the saturation chamber and subjected first to brine imbibition under vacuum (~10^{-4} Pa), followed by a 5 MPa pore fluid pressurization to enhance the dissolution of any remaining air in the porous media. The test was performed at constant confining pressure (P_c) of 40 MPa at room temperature (~19.5 °C), while pore pressure downstream (P_{down}) was set to 9.5 MPa. Because the experiment was performed under constant flow conditions, pore pressure upstream (P_{up}) was not constant and, on average, it attained a value of 11±1 MPa during the experiment. The pore pressure difference up- and downstream ($\Delta P_p = P_{up} - P_{down}$) of the sample, temperature (T), and axial (ε_a) and radial (ε_r) strains were measured every second. Electrical resistivity was systematically measured at least every one sample pore volume (1PV ~10 ml) time of flow-through.

During the drainage stage of the experiment the volume fraction of CO_2 (X_{CO_2} = V_{CO_2} (V_{CO_2} + V_{H_2O})$^{-1}$; being fraction of brine X_w = 1 - X_{CO_2}) was increased from 0 to 1 in 0.2 X_{CO_2} units, stepwise. For the imbibition, we set up a continuous flow-through with brine. From Batzle and Wang (1992) relationships, the density and viscosity for CO_2 are 864 kg m^{-3} and 8.64 10^{-5} Pa s, respecitively, and 1026 kg m^{-3} and 1.084 10^{-3} Pa s for the brine, for the physicochemical (*P*-*T*-salinity) conditions imposed in the test. We imposed a condition of maximum ΔP_p = 2 MPa, to keep CO_2 viscosity and density variations across the sample below 5%. To satisfy this condition, in the beginning of each flow-through episode the total flow ($Q_{T,IL}$ = Q_w + Q_{CO_2}; the subscript 'IL' refers to flow inlet) was regulated between 0.1 and 0.5 mL min^{-1} (accepted values for field flow rates (Berg et al., 2013)), and kept constant until the next episode.

The injection of pure fluids (either brine or CO_2) was possible with dedicated pumps and the fluid transfer vessels described above. To inject the mixed fluid we used a ~4.5 m of 1/16" stainless steel high pressure tubing (0.1651 mm ID). The length of the pipe coupled with its inner surface roughness and its sinuosity (coil-type) enhance homogeneous mixing and sufficient time of interaction (El-Maghraby et al., 2012; Farajzadeh et al., 2009). The reciprocal solubilities of CO_2 and brine for the physicochemical conditions prevailing in the test are ~6.8 vol.% CO_2 in brine, and < 0.1 vol.% brine in CO_2 (Canal et al., (2013), based on the equations of Duan et al. (2006)). Considering these values, the actual X_{CO_2} and X_w were corrected by subtracting the corresponding dissolved mass components, whereas the criterion for steady state was assumed by the condition of corrected inflow equal to outflow (Dullien, 1992).

3. Permeability, electrical resistivity and degree of saturation

3.1. Absolute and relative permeability

The absolute permeability (k_{abs}) to brine was calculated at the initial brine-CO_2 flow episode (X_w = 1) before starting CO_2 injection. During this period the sample was completely saturated with brine. k_{abs} was derived using the steady-state flow method based on Darcy's law:

$$k_{\mathrm{abs}} = \frac{\mu Q L}{\Delta P_{\mathrm{p}} A}, \quad (1)$$

where μ is the dynamic viscosity of the fluid (Pa s), Q is the volumetric flow rate ($m^3 s^{-1}$), ΔP_p is the pressure drop across the sample (Pa), A and L are the cross sectional area (m^2) and the length (m) of the sample, respectively.

We calculated relative permeability to brine and CO_2 (denoted hereafter as $k_{r,w}$ and k_{r,CO_2}, respectively) by simultaneously circulating both fluids (with different volume ratios) at controlled pore pressure and flow rates, using a two-phase multiphase flow system (Dullien, 1992):

$$k_{\mathrm{r,i}}(S_{\mathrm{i}}) = \frac{\mu_{\mathrm{i}} Q_{\mathrm{i}} L}{\Delta P_{\mathrm{p}} A k_{\mathrm{abs}}} \quad (2)$$

In Eq. (2), the relative permeability of each phase (denoted with the subscript *i*) is a function of their partial contribution to the total saturation, inferred from the electrical resistivity of the sample as explained below. Partial fluid mobility is controlled by the relative permeability of each fluid phase.

3.2. Two-phase relative permeability models

Multiphase flow properties are needed to characterize the mobility of the CO_2 plume, the injection pressure, the extent of the residual CO_2 trapping and the far-field pressure distribution (Krevor et al., 2012; Müller, 2011).

Several empirical relationships for relative permeability in multiphase systems have been developed. The Brooks-Corey's model is the one more generally used to describe relative permeability curves in water-CO_2 systems (e.g., Krevor et al. (2012), Bachu (2013)), although the Corey's (Corey, 1954), Purcell's (Purcell, 1949) or van Genuchten's (van Genuchten, 1980) models are also applied (e.g. Li and Horne (2006), Oostrom et al. (2016)). Multiphase flow simulators such as TOUGHREACT (Xu et al., 2017), ICSSM (Shi et al., 2007) or METSIM2 (Shi et al., 2011), use van Genuchten and Corey models to solve relative permeabilities to water and gas, respectively.

Purcell's model tends to give better fits for the wetting phase, while Corey's and Brooks-Corey's models seem to be appropriate for both phases (Li and Horne, 2006). Based on this, we compare our experimentally obtained relative permeability curves to those from the modified version of Brooks-Corey in Krevor et al. (2012) for the wetting (brine) and non-wetting (CO_2) phases, with the Purcell and van Genuchten models for the wetting phase, and the Corey model for the non-wetting. These models use the normalized water saturation (S_w^*) to calculate the relative permeability:

$$S_{\mathrm{w}}^{*} = \frac{S_{\mathrm{w}} - S_{\mathrm{wr}}}{S_{\mathrm{e}}}, \tag{3}$$

where S_w is the degree of water saturation, S_{wr} is the residual water saturation, and S_e is the effective saturation, that is, the saturation in the sample within the range which is still available to be saturated. For drainage $S_e = 1 - S_{wr,}$ while for imbibition $S_e = 1 - S_{wr} - S_{CO_2r,}$ where S_{CO_2r} is the residual CO_2 saturation. At $S_{wr,}$ the relative permeability to CO_2 is maximum. During imbibition, as water saturation increases, k_{r,CO_2} decreases until it reaches its minimum at S_{CO_2r}. The equations and parameters of each model are presented in Table 2.

Table 2. Relative permeability models (A: Purcell (1949); B: Corey (1954); C: Krevor et al. (2012); D: van Genuchten (1980)). In models A and D, λ is the pore size distribution index; in model C, N_w and N_{CO_2} are the Corey exponents for the wetting and non-wetting phase, respectively. See the text for explanation of other parameters.

Models	Wetting phase (brine, $k_{r,w}$)	Non-wetting phase (CO_2, k_{r,CO_2})
Purcell (A)	$k_{\mathrm{r,w}} = (S_{\mathrm{w}}^*)^{\frac{2+\lambda}{\lambda}}$	
Corey (B)		$k_{\mathrm{r,CO_2}} = (1 - S_{\mathrm{w}}^*)^2[1 - (S_{\mathrm{w}}^*)^2]$
Brooks-Corey (C)	$k_{\mathrm{r,w}} = (S_{\mathrm{w}}^*)^{N_{\mathrm{w}}}$	$k_{\mathrm{r,CO_2}} = k_{\mathrm{r,CO_2}}^{\max}(1 - S_{\mathrm{w}}^*)^2[1 - (S_{\mathrm{w}}^*)^{N_{\mathrm{CO_2}}}]$
van Genuchten (D)	$k_{\mathrm{r,w}} = \sqrt{S_{\mathrm{w}}^*}\left[1 - \left(1 - S_{\mathrm{w}}^{*\,1/\lambda}\right)^{\lambda}\right]^2$	

3.3. Electrical resistivity

Archie's first and second laws (Archie, 1942) allow to relate electrical resistivity to brine saturation in variably saturated clean (clay-free) reservoir rocks (Mavko et al., 2009). Archie's first law relates the formation factor of the rock, F_0, to the porosity (ϕ) of the porous medium when fully saturated, as follows:

$$F_0 = \frac{R_0}{R_{\mathrm{w}}} = \emptyset^{-\mathrm{m}}, \tag{4}$$

where R_0 and R_w are the resistivities of the (fully saturated) rock and pore fluid, respectively, and m the cementation exponent.

Archie's second law extends the previous relationship to partially saturated rocks, through the following expression:

$$S_{\mathrm{w}} = \left(\frac{R_{\mathrm{w}}}{\emptyset^m R_{\mathrm{b}}}\right)^{1/n}, \tag{5}$$

where R_b is the bulk electrical resistivity of the rock, and n is the saturation exponent. The empirical exponents m and n usually adopt values close to 2 for

sandstones (Mavko et al., 2009). This relationship is useful to describe fluid substitution in brine-CO_2-rock systems initially saturated with the conducting fluid (brine), where the resistivity increases when brine is replaced by the non-conductive CO_2 phase. CO_2 saturation (S_{CO_2}) is computed as the reciprocal of brine saturation (i.e., $S_{CO_2} = 1 - S_w$).

For a reservoir with low chemical reactivity to CO_2 (e.g., silicic sandstones), R_w can be assumed to be constant. Then, we can normalize the bulk resistivity in terms of partial formation factors (F_i), as follows:

$$F = \frac{F_0}{F_i} = \frac{R_0}{R_b} = S_w^n, \quad (6)$$

Our normalized formation factor F is the inverse of the resistivity index (e.g., Dullien (1992)). Using Eq. (6), the S_w in the conventional relative permeability curves can be directly replaced by the measured property (F), by adjusting the saturation exponent n (e.g., Li (2008)). In this contribution, we analyse our experimental results from this angle, assuming that the system remains chemically non-reactive to CO_2-brine-rock interaction, so that the bulk electrical resistivity of the rock is solely function of the partial saturation of each fluid phase in the porous medium.

Some models account for the excess of conductivity induced by the presence of clay minerals by introducing an additional term into Archie's law (Mavko et al., 2009). However, here we neglect this effect due to the practical absence of clays, which is limited to the kaolinite used to make the rock and practically consumed in the manufacturing process (Tillotson et al., 2012).

4. Results

Pore pressure difference (ΔP_p) progressively increases (the pressure upstream, P_{up}, goes up; the pressure downstream, P_{down}, remains constant) as the volume fraction of CO_2 (X_{CO_2}) increases (Figure 2), during the first two fractional flow episodes (up to X_{CO_2} = 0.4). Thereafter, the inlet flow rate ($Q_{T,IL}$) is reduced by 50% down to 0.25 mL min^{-1} to satisfy our imposed condition of ΔP_p < 2 MPa and keep the CO_2 variations in density and viscosity below 5% across the sample. The reduction in the inlet flow rate decreases the ΔP_p for the next three drainage episodes. During imbibition, we imposed the same flow rate as that used during the first (X_{CO_2} = 0) injection episode (i.e. 0.5 mL min^{-1}). However, ΔP_p is higher during imbibition than during the original drainage (100% brine) episode (i.e., more energy required to flow-through), which can be related to the presence of a residual CO_2 fraction in the porous medium. During drainage, the presence of CO_2 increases the data dispersion of the resulting flow downstream ($Q_{T,OL}$; the subscript 'OL' refers to flow outlet), which decreases towards the end of each episode, eventually satisfying the condition $Q_{T,OL} = Q_w + Q_{CO_2}$ (after discounting mutual phases dissolution fractions).

Assuming a good gauge-rock function during the test (i.e., no visual damage evidences), volumetric strain (ε_v) was inferred from axial (ε_a) and radial (ε_r) strains ($\varepsilon_v = \varepsilon_a + 2\varepsilon_r$). We observe no significant changes in the dimensions of the sample during the major part of the experiment, although some axial and minor radial increase were recorded after attaining X_{CO_2} = 0.6. At the end of the experiment, the maximum volumetric strain computed reached ~0.13% (i.e., axial and diametrical enlargement of ~0.06 and ~0.025%, respectively; Figure 2). At the sample scale, that corresponds to an apparent swelling of ~12 μm in both the axial and diametric directions. Strains

remained constant during imbibition. The magnitude of the swelling is small and rather intriguing, considering the significant confining pressure and nearly constant (average) pore pressure conditions, and the absence of swelling minerals.

The resistivity gradually increases with CO_2, by ~300% at the end of the X_{CO_2} = 0.8 episode (Figure 2). Then, the sharpest increase (~500%) occurs with pure CO_2 flowing through the sample (X_{CO_2} = 1), indicating that high CO_2 saturations are needed to effectively block the conductive connections. This behaviour is different to the gradual transition reported by Falcon-Suarez et al. (2017) for a sample with homogeneous pore shapes. During imbibition, brine partially refills the pore space and resistivity drops down to ~10% above its original value, likely related to CO_2 trapping in the porous medium.

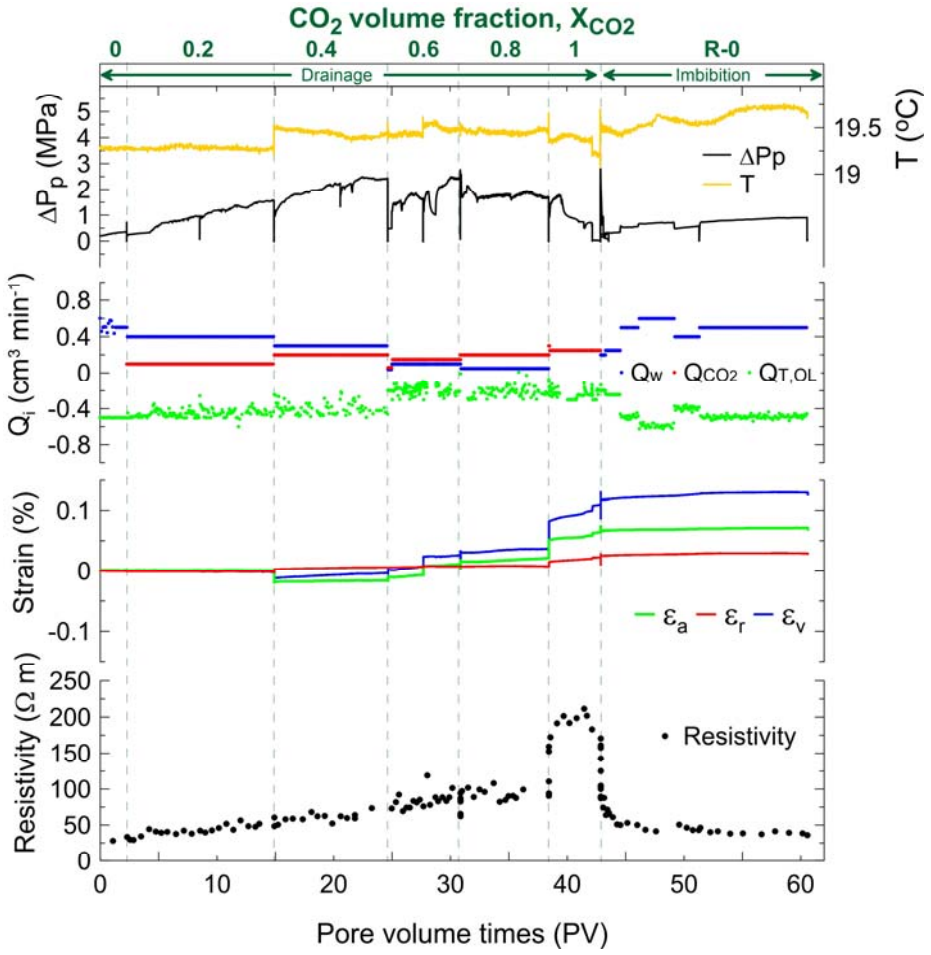

Figure 2. Brine-CO_2 flow-through test on 45A synthetic sandstone with a controlled distribution of non-connected fractures. Pore pressure difference (ΔP_p), temperature (T), partial flows for CO_2 (Q_{CO_2}), brine (Q_w) set upstream and the resulting fluid flow outlet ($Q_{T,OL}$) downstream, axial, radial and volumetric strains (ε_a, ε_r *and* ε_v, respectively), and electrical resistivity for seven consecutive brine-CO_2 injection stages denoted as volume fractions of CO_2 (X_{CO_2}, see text for details), covering six drainage (from X_{CO_2} = 0 to X_{CO_2} = 1) and a forced imbibition (X_{CO_2} = R-0) episodes, plotted versus pore volume (PV). Vertical dashed lines separate consecutive brine-CO_2 stages. Notice that we only show effective flow time; interludes between two consecutive episodes are omitted. The duration of the interludes varied from one episode to the next, as follows: $X_{CO_2,[0-0.2]}$ ~0.1 h; $X_{CO_2,[0.2-0.4]}$ ~15 h; $X_{CO_2,[0.4-0.6]}$ ~0.1 h; $X_{CO_2,[0.6-0.8]}$ ~13 h; $X_{CO_2,[0.8-1]}$ ~13 h; and transition from drainage to imbibition, $X_{CO_2,[1-R-0]}$, ~40 h.

1

5. Data assessment

5.1. Relative permeability versus resistivity

Both the wetting (brine) and non-wetting (CO_2) phase curves (Figure 3) fit power-functions of the form $k_{r,i} = aF^b$, where a and b are the fitting parameters (Table 3) and the subscript i denotes the fluid phase. The relative permeability curves estimated by Purcell (P), Brooks-Corey (BC) and Van-Genuchten (vG) models for the wetting phase, and by Corey (C) and Brooks-Corey (BC) models for the non-wetting phase, were obtained (sample 45A; Table 3) by using $S_w = F^{1/n}$ with a saturation exponent n of 2, a value commonly accepted for sandstones (Mavko et al., 2009).

For the wetting phase, Brooks-Corey and Purcell models are in a better agreement with our experimental data than the van Genuchten model; for the non-wetting phase, only Brooks-Corey model fits reasonably well (Figure 3). Nonetheless, differences between the theoretical models and the experimental fits can be related to the heterogeneous distribution of pore shapes in our sample, an aspect neglected by these models (Müller, 2011).

The crossing point of the relative permeability curves (i.e., $k_{r,CO_2} = k_{r,w}$) is a function of the wettability of the sample (Reynolds, 2016). In our experiment, it occurs at F ~0.23 (Figure 3), equivalent to S_{CO_2} ~0.52, which suggests that the non-wetting phase preferentially adheres to the grain surface (Reynolds et al., 2018). The extremely low k_{r,CO_2} end-point also suggests low mobility, which may be indicating either a high IFT between CO_2 and brine and/or a pore structure less favourable for uniform displacement (Bennion and Bachu, 2006). The imbibition data evolution in Figure 3 reflects that the formation factor increases with very low relative permeability variations. Since the injected brine is unsaturated in CO_2, this trend would be indicating

fast CO_2 dissolution (< 3 PV, equivalent to < 1 h at the experimental conditions; Figure 2) until the residual CO_2 saturation is achieved ($S_{CO_2,r}$ ~0.15).

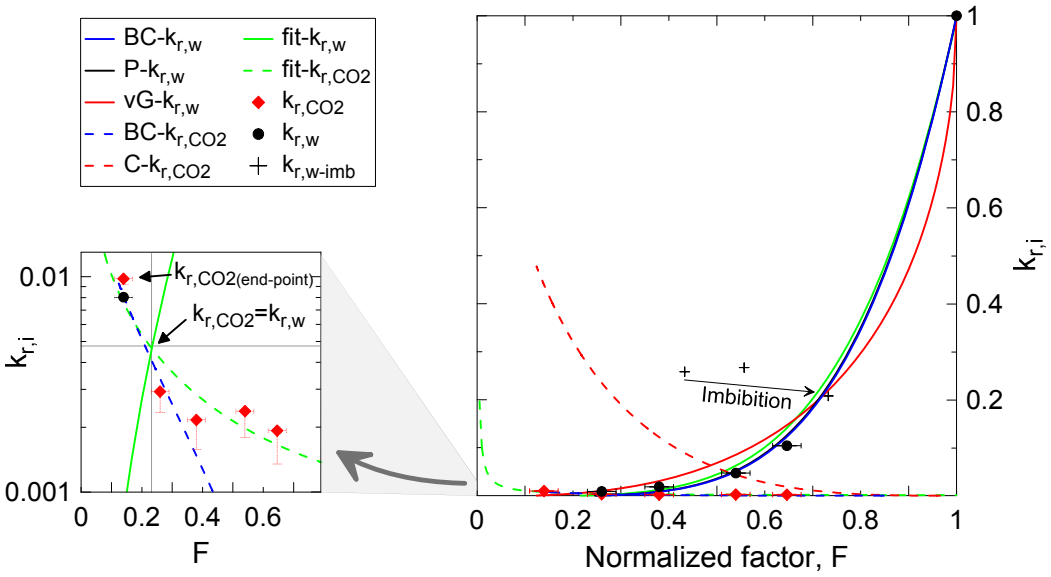

Figure 3. Brine-CO_2 relative permeability ($k_{r,i}$) versus normalized formation factor (F), from drainage (dots for $k_{r,w}$; diamonds for k_{r,CO_2}) and imbibition (crosses for $k_{r,w\text{-}imb}$; the arrow labelled "imbibition" indicates the data evolution) experimental data for the fractured synthetic sandstone. The graph includes the best fit curves for the wetting (fit-$k_{r,w}$) and non-wetting (fit-k_{r,CO_2}) phases based on the experimental data, together with the best fit curves for Brooks-Corey (BC-$k_{r,w}$), Purcell (P-$k_{r,w}$) and van Genuchten (vG-$k_{r,w}$) models for the wetting phase, and Brooks-Corey (BC- k_{r,CO_2}) and Corey (C- k_{r,CO_2}) models for the non-wetting phase, with best-fit parameters given in Table 3. The inset plot shows the crossing point for $k_{r,w}$ and k_{r,CO_2} based on the experimental data. The error cross bars arising from the experimental data correspond to the uncertainty propagation from the electrical resistivity measurements (horizontally) and the CO_2 dissolution and viscosity variations across the sample in the relative permeability (vertically).

The specific dimensions of the sample, together with the experimental procedure applied, may be affecting our observations. We expect significant capillary end effects (Leverett, 1941) because of the low length-to-diameter ratio (slenderness) of our rock

sample, which result in heterogeneous pore pressure and fluid distributions across the plug. Based on the characterization developed by Jackson et al. (2018), neglecting this boundary effect can lead to a crossing point underestimation of up to one order of magnitude in relative permeability and ~5% in saturation, for our experimental conditions. This aspect limits the extrapolation of our observations regarding the fractures effect on fluid mobility and CO_2 storage capacity to samples with similar geometric characteristics tested at similar experimental conditions.

We compare our results to those obtained from three previous experiments (Falcon-Suarez et al., 2017, 2016; Papageorgiou et al., 2018) performed with non-fractured synthetic sandstones using a similar experimental approach. The datasets of these tests are available at the http://www.bgs.ac.uk/discoveryMetadata/. These synthetic sandstones were made using similar manufacturing conditions and materials to those employed in this study, but with variable sand-to-cement ratios. Consequently, the resulting samples S026 (Falcon-Suarez et al., 2016), S038 (Falcon-Suarez et al., 2017) and S045 (Papageorgiou et al., 2018), have different porosities (0.26, 0.38 and 0.45, respectively) and permeabilities (1, 50 and 500 mD, respectively). Considering that all samples have the same grain size and that they were subjected to the same consolidation during manufacturing, the pore size distribution of the three non-fractured samples should be similar but with different cumulative distribution (Falcon-Suarez et al., 2019). Then, the main difference in terms of transport properties should be the presence of fractures. All the experiments were performed at the same brine salinity (35 g L^{-1} NaCl). The main differences with respect to our test are the temperature, which was set above 31 ºC and the variable pore pressure from 7 to 12 MPa (seeking for supercritical-CO_2 conditions). The latter condition caused significant data scattering in the relative permeability values (Falcon-

1 Suarez et al., 2016). Also, although the three experiments present drainage episodes,

2 imbibition is only available for S038 (Falcon-Suarez et al., 2017).

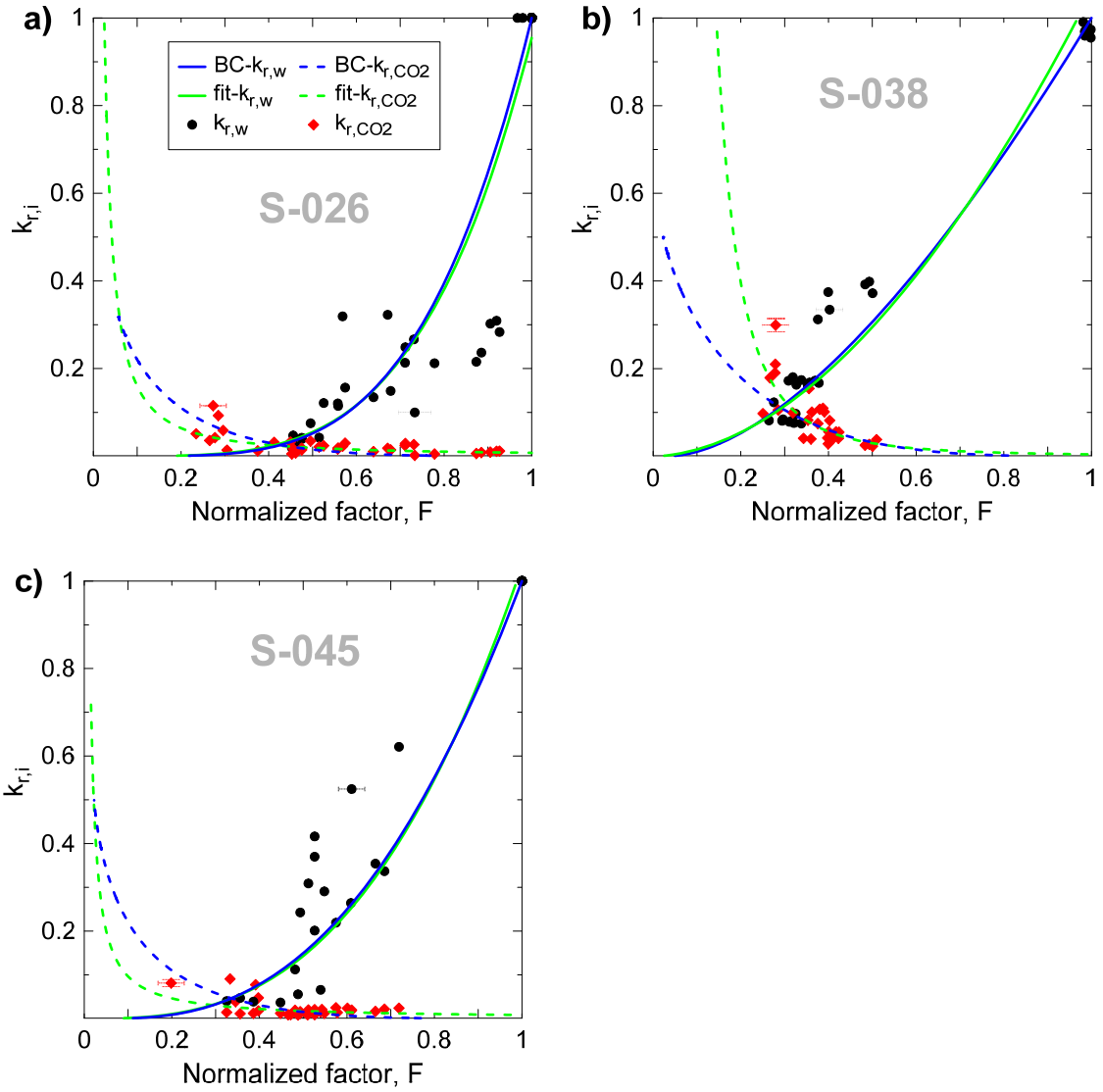

Figure 4. Brine-CO_2 relative permeability ($k_{r,i}$) versus normalized formation factor (F). Experimental data for the brine ($k_{r,w}$) and CO_2 (k_{r,CO_2}) phases for the three non-fractured synthetic sandstones: (a) S026; (b) S038; (c) S045 (Falcon-Suarez et al., 2017, 2016; Papageorgiou et al., 2018). The plot includes the best fit curves for the wetting (fit-$k_{r,w}$) and non-wetting (fit-k_{r,CO_2}) phases based on the experimental data, together with the best fit curves for Brooks-Corey for the wetting (BC-$k_{r,w}$) and non-wetting phases(BC-k_{r,CO_2}), with best-fit parameters given in Table 3. To facilitate the visualization, only one error cross bar is displayed: The horizontal bar covers the error associated with the electrical resistivity; the vertical bar, the influence of the (neglected) dissolved CO_2 in the relative permeability.

3

As above, we fit the data using power-functions of the kind $k_{r,i} = aF^b$ for both the wetting and non-wetting phases (Table 3 and Figure 4). Based on the results obtained for the fractured sample, we only account for Brooks-Corey to fit the non-fractured samples data. For S038 and S045 the measured relative permeabilities are higher than those from the models for intermediate *F* values (within the range 0.35 - 0.75).

Table 3. Fitting parameters for Brooks-Corey (BC), Purcell (P) and van Genuchten (vG) models for the fractured sample (45A), the BC for the three non-fractured samples (S026, S038, S045), and power-function experimental fitting for the four samples.

*Fitting parameters	Fractured sample	Non-fractured samples		
	45A	S026	S038	S045
Brooks-Corey				
N_w	7.5	7	2.8	4.5
N_{CO_2}	0.1	0.7	1.8	0.7
Purcell				
λ_P	0.3			
van Genuchten				
λ_{vG}	0.55			
BC, P, vG				
S_{wi}	0.1			
k_{r,CO_2}	0.4			
Experimental fit ($k_{r,w}$ | k_{r,CO_2})				
a	0.95 | 1_x10^{-3}	0.97 | 3_x10^{-3}	1.05 | 7_x10^{-5}	1.05 | 1_x10^{-3}
b	4.02 | 1.38	4.13 | -2.30	1.84 | -6.82	2.87 | -3.48
R^2	0.97 | 0.27	0.91 | 0.26	0.90 | 0.70	0.88 | 0.30

* The values were derived from an iterative, error constrained least square fitting.

5.2. Hydrodynamic modelling

In Falcon-Suarez et al. (2017), the geochemical analysis of the pore fluid revealed a gradual reduction of the major cation Na with increasing CO_2, interpreted as salt precipitation phenomena during CO_2-injection. To assess the hydrodynamics

of our test, including potential CO_2-induced salt precipitation/dissolution effects, we performed a 2D axisymmetric radial numerical simulation of our experiment using TOUGHREACT v3.3 code (Xu et al., 2017). TOUGHREACT is a non-isothermal reactive transport code that introduces reactive chemistry into the existing multi-phase fluid and heat flow code TOUGH2 (Xu et al., 2017, 2004). TOUGHREACT uses a fluid property module called ECO2N designed for applications to CO_2 storage in saline aquifers (Pruess, 2005). This module reproduces fluid properties of H_2O-NaCl-CO_2 mixtures under temperature, pressure and salinity conditions typically encountered in storage reservoirs of interest (10ºC ≤ T ≤ 100ºC; P ≤ 60 MPa; salinity up to halite saturation). Here, we consider that the system is chemically non-reactive to CO_2-brine-rock interaction and only solve the multiphase fluid transport processes (find the details of the modelling in Appendix A).

CO_2 extends laterally and vertically from the injection point, and after the first CO_2 injection episode (X_{CO_2} = 0.2), the upward migration of CO_2 occurs quickly and S_{CO2} reaches ~0.15. The maximum S_{CO2} of ~0.35 is achieved after the last drainage episode (X_{CO_2} = 1) (Figure 5). The model reported no evidences of salt precipitation at the experimental conditions. The maximum S_{CO_2} obtained in the model (S_{CO_2} ~0.35) significantly differs from that estimated from electrical resistivity, S_{CO_2} ~0.55. From this 20% difference, the combined effect of the resistivy error and the empirical saturation factor (n = 2) used for the conversion (see above) could explain ~10% variability in saturation. The remaining 10% could be related to the pore fabric of the rock. Since the model does not reproduce the non-connected fractures, we interpret this 10% represents CO_2 preferentially trapped in the fractures (see discussion below).

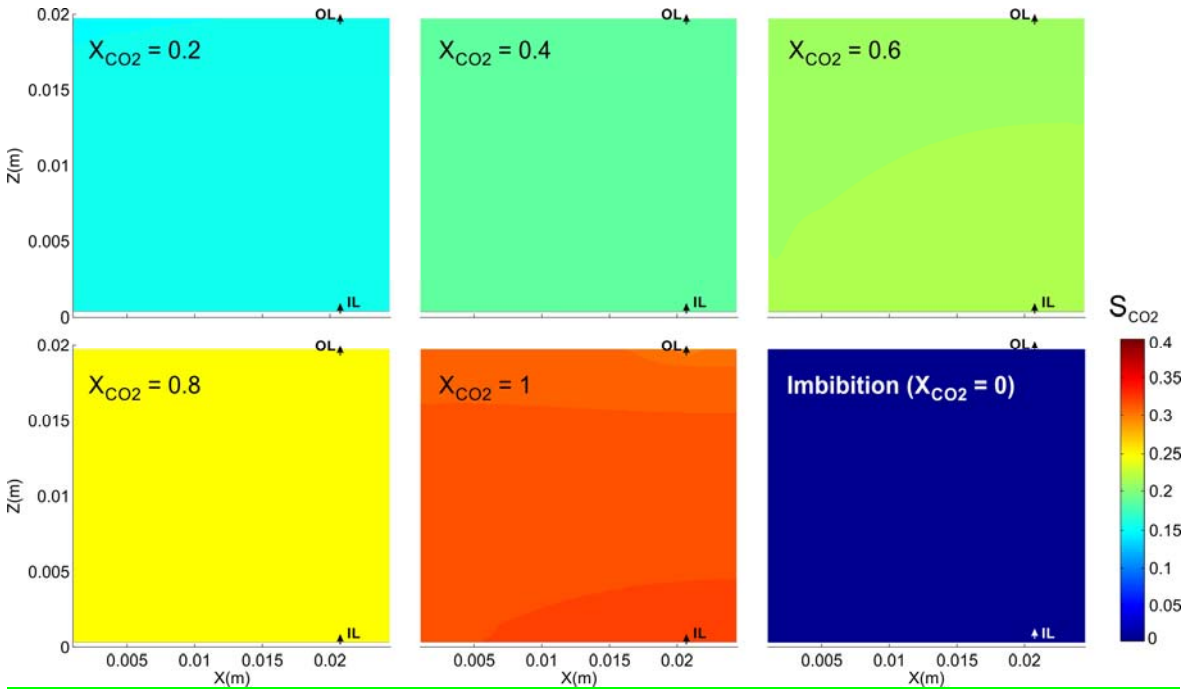

Figure 5. Distribution of CO_2 saturations (S_{CO_2}) within the sample after five drainage episodes (from X_{CO_2} = 0.2 to X_{CO_2} = 1). For the first drainage episode and imbibition (X_{CO_2} = 0 in both cases) the sample was fully saturated in brine. The horizontal (x) and vertical (z) axis are the sample radius and thickness, respectively. The symmetry axis of the sample is placed at x = 0, and the flow inlet (IL) and outlet (OL) points are ~21 mm far from it, at the bottom and the top of the sample, respectively.

6. Discussion

6.1. Hydro-mechanical interpretation

The reactivity of our synthetic sample is very low, but may be able to induce an increase in porosity and permeability (Hangx et al., 2015). Post-test porosity (ϕ_f) and gas permeability ($k_{gas,f}$) were measured after a week of immersion in DIW; porosity increased from 0.273 to 0.296 (~8% increment) and permeability increased from 5.5 to 12.1 mD (~54% increment). These changes indicate rock weathering during the flow-through experiment, linked to the dissolution of mineral phases or to mechanical damage associated with crack propagation; probably both (e.g., Hangx et al., 2015).

In principle, the low-concentrated (10% HCl) acid solution used originally for dissolving aluminium disks in the sample to create the fractures, should have had a minor effect on the rock matrix, composed by quartzose grains and silica cement. However, this sample was previously used to study stress-induced changes and partial saturations effects on ultrasonic properties of fractured media (Amalokwu et al., 2015; Tillotson et al., 2012). The variable stress history applied in those experiments may have also contributed to develop localized weak points in the microstructure, resulting in grain-to-grain bounds weakening from one test to the next, explaining the porosity and permeability variations.

To characterize the microstructure of the sample, we segmented it into smaller portions to obtain two oriented thin sections: normal and parallel to the dip direction of the cracks (Figure 6). The thin sections reveal distinct stress-induced features. For instance, section A-A” (Figure 6b), which represents the dip direction of the crack, illustrates that, locally, the major axis of the crack ellipsoid has been enlarged by a factor of 2 with respect to its original nominal size. This effect might be attributed to Al-disk overlaping during the manufacturing process (Tillotson et al., 2012), but also to crack propagation. Eventhough the cracks have grown, they remain non-connected. This observation suggests the permeability changes from before to after the test are not related to flow paths enhancement, or at least they would be very difficult to explain using a continuum media approach (Lee et al., 1999). Grain scale arching effects are also present (Figure 6c), indicating local heterogeneous load distribution (Falcon-Suarez et al., 2019). We also observe that some small-scale horizontal cracks appear to have formed at or close to the crack tips (Figure 6b).

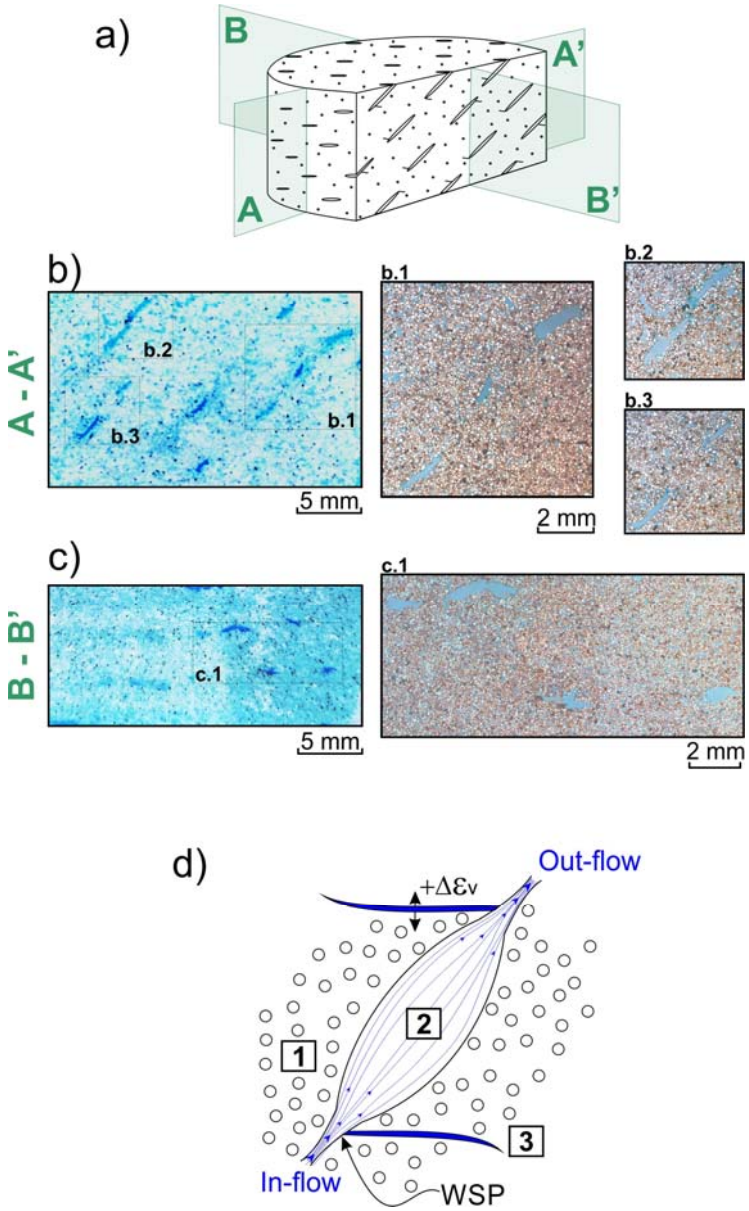

Figure 6. (a) Schematic of the synthetic sample with a controlled distribution of non-connected fractures aligned at 45º from its axis. (b) Thin section parallel to fracture dip and (c) thin section perpendicular to fracture plane. (d) Conceptual model of the porous medium, consisting of three different pore families: (1) porosity, (2) aligned penny-shape fractures, and (3) microcracks.

1

2 Based on the previous observations, we describe a conceptual model for brine-
3 CO_2 multi-flow through non-connected fractured rocks (Figure 6d). The model
4 identifies three pore families: (1) intergranular space (i.e., catenary pores); (2) non-

connected, aligned penny-shaped voids or isolated cracks; and (3) microcracks, associated with stress-variations from the original formation properties.

The dimensions and distribution of the fractures, and the matrix porosity were prescribed by the manufacturing process. However, additional microcracks could have been also generated during block coring and/or along the various stress-paths to which the plug was submitted prior to our experiment (Amalokwu et al., 2015; Tillotson et al., 2012). Abrupt geometric changes, such as the transitions between pores and fractures (Pollard and Aydin, 1988), may cause a localized increase in stress. At these weak structural points (WSP, Figure 6d), microcracks are also prone to develop and propagate when the level of stress reaches the critical strength of the material.

The observed volumetric deformation (~0.12%) is within the 0.7% porosity fraction commonly attributed to microcraks (Fortin et al., 2007). Microcracks partially close during loading as the confining stress is gradually increased (Fjaer et al., 2008). When the sample is originally saturated in brine, the microcracks turn into capillary fringes while closing. If the closure process is incomplete, then the brine in the capillary fringes remains immobile during CO_2 injection, due to the high surface tension of the wetting phase (Kim et al., 2013). Then, effective stress changes within the sample could explain the strain evolution observed during the test.

During CO_2 injection, when pore pressure increases for a constant confining stress, the drop in effective stress may result in rock dilatancy and crack movement. The former can explain the axial strain increase, while the latter would lead to a more complex deformation pattern, preferentially affecting the radial deformation. For hydrostatic stress conditions the orientation of our artificial cracks (45º) should be adequate to compensate in an equally proportioned way the fluctuations in pore pressure. However, misalignments in the manufacturing process may have result in

crack orientation at angles different to 45º that could lead to variable stress concentration effects along the sample, and eventually to radial strain increase.

6.2. Effects and implications of non-connected fractures in CO_2 storage reservoirs

A number of methods have been developed to measure the wettability of a rock-fluid system (Castillo et al., 2011). Among them, relative permeability curves can be used to qualitatively assess strong changes in wettability, although minor differences may remain unnoticed (Dandekar, 2013). Our fractured sample (45A) shows a relative permeability cross point at F ~0.23 (Figure 3), which may be indicating a weaker water-wet behaviour than the non-fractured samples (S026, S038 and S045) with F values within the range of 0.32-0.38 (Figure 4). This observation suggests the pore morphology may affect the wettability of the sample, although the differences between the cross points may be insufficient to guarantee this behaviour. The residual trapping is also indicative of wettability. Our data for residual trapping are only available for samples S038 (Falcon-Suarez et al., 2017) and 45A, with S_{CO_2r} ~0.16 and ~0.15, respectively. These two close values would indicate similar wettability in both cases, although the lack of imbibition data for S026 and S045 limit any further interpretations.

Although water-wet rocks are desirable CO_2 reservoirs, the degree of trapping also depends on other aspects besides wettability, such as pore to throat size ratio, connectivity and flow rate. The pore scale physics of trapping is governed by the competition between snap-off of wetting layers and piston-like advance (Krevor et al., 2015). During piston-like filling, a displacing phase progressively fills the pores and throats, gaining space over the other phase and forcing it to exit the pore space. Snap-off occurs as the wetting phase on the pore wall and corners swells and separates two pores filled with the non-wetting phase, disconnecting and trapping the non-wetting

phase in the centre of the pores. This process only occurs if the movement of the wetting phase is prevented by very large pores (Krevor et al., 2015), as in our 45A sample. Accordingly, we interpret that the poorly connected fracture network of our 45A sample facilitates the isolation of the non-wetting phase and benefits the CO_2 trapping in the porous medium, when compared to non-fractured samples.

The data of the four samples compared here were obtained from experiments performed at the same brine salinity (35 g L^{-1} NaCl), but different *P-T* conditions. The mean pore pressure observed in the 45A test (i.e., P_p = 11 ±1 MPa) is within the upper P_p range (7 to 12 MPa) applied for the tests performed on the three non-fractured samples S026, S038 and S045 (Papageorgiou et al., 2018). Therefore, the most significant difference between experiments is the temperature: room temperature at 19 °C for the 45A sample, 35 ºC for S026 and S045, and 32 ºC for S038 (i.e., supercritical CO_2 conditions for the non-fractured samples). Hence, a relatively lower water wettability might be expected in the 45A sample because the temperature difference between experiments would decrease the CO_2-brine interfacial tension by ~15% (Bachu and Bennion, 2009). The higher IFT of the non-fractured samples would lead to increase the convexity of the relative permeability curves (Bachu and Bennion, 2008), and to lower the endpoint relative permeability value (Bennion and Bachu, 2006). However, we observe the contrary, which suggests the IFT might have a minor effect on our results.

The end-point relative permeability to CO_2 significantly controls injectivity (Yoshida et al., 2016). The extremely low k_{r,CO_2} in the 45A sample suggests that the presence of fractures is affecting the mobility of the individual phases (brine and CO_2), when compared to the non-fractured samples. This interpretation agrees with the observations reported by Reynolds and Krevor (2017), of CO_2 preferentially filling high

porosity layers in heterogeneous cores. In our experiment, in essence, the lower capillary entry pressure of the large pores (fractures) benefits the displacement of the wetting phase by the non-wetting one, allowing the CO_2 to fill the large fractures, preferentially. During imbibition, the CO_2 would remain trapped in the fractures due to their lower capillary pressure, provided that they are non-connected.

With certain limitations (arising from sample size and the non-random orientation of fractures), we speculate our fractured sample represents a scaled-down ideal reservoir with non-connected fractures. Our experimental results suggest that this type of reservoirs could potentially isolate the CO_2 fraction in the central section of the fractures. This finding might have significant implications in the storage efficiency. Although CO_2 mobility would be reduced in non-connected fractured systems, the fractures would be acting as small reservoirs, enhancing the overall CO_2 storage efficiency of the system. Based on these observations, an ideal configuration for a potential CO_2 storage site could be a reservoir in which (i) the bottom part of the formation (injection point) has high CO_2 mobility (i.e., a porosity/permeability formation, which could contain interconnected fractures), to guarantee an adequate injectivity and distribution of the CO_2 plume, and (ii) the top part has non-connected fractures that would act as vertical flow barriers, helping to immobilize the CO_2 plume and enhancing the whole trapping efficiency of the reservoir (Figure 7).

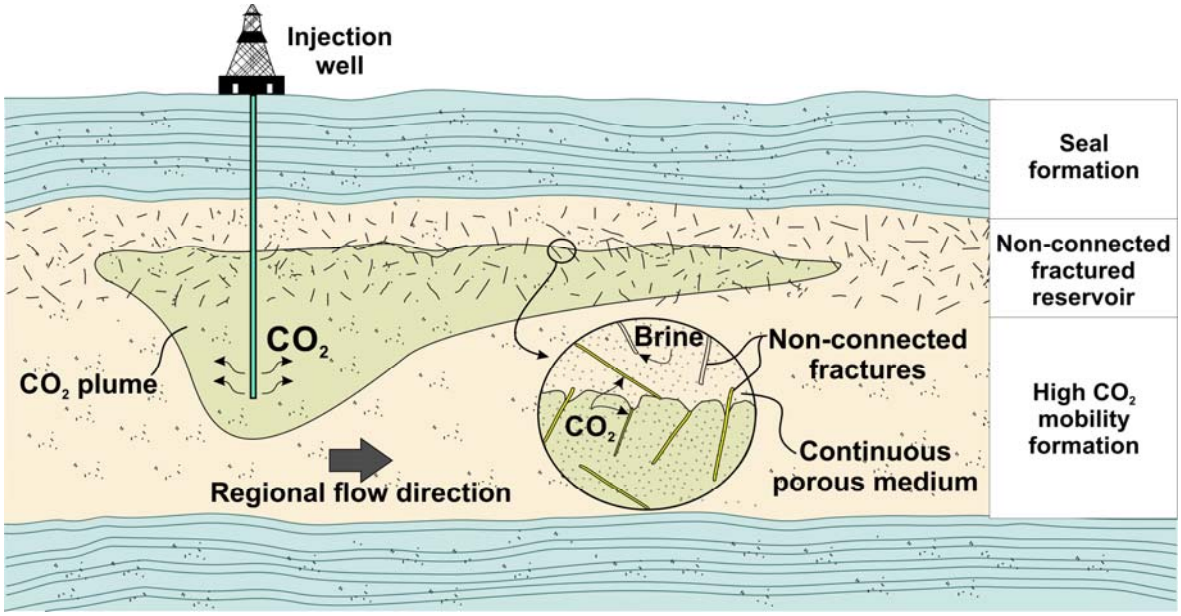

Figure 7. Schematic diagram of an ideal CO_2 storage reservoir, showing CO_2 injection and plume migration. The bottom part of the reservoir is a non-fractured formation with high CO_2 mobility, allowing efficient injection and distribution of CO_2. Above this formation, a non-connected fractured layer with high CO_2 trapping capacity immobilises the CO_2 plume.

7. Conclusions

We have performed a brine-CO_2 flow-through experiment using a synthetic sandstone sample with oblique aligned cracks while monitoring electrical resistivity and relative permeability. The experimental results have been compared to previous experiments in which similar synthetic samples without cracks were tested under similar conditions. Based on the newly obtained experimental data, the integration of previous results and rationale described in the text we conclude that:

- The presence of non-connected fractures may hamper the mobility of CO_2 in the porous medium and slightly increase the residual CO_2 trapping.
- In a weak water-wet sample, large fractures may prevent the movement of the wetting phase and facilitate the partial isolation of the non-wetting phase in the

centre of pores (snap-off process). Further experiments to investigate the wettability on fractured samples are required for more robust interpretations.

- Heterogeneities within the porous medium may lead to differences among the various relative permeability models. The Brooks-Corey's model can be used to describe relative permeability curves for the wetting and non-wetting phase, in both fractured and non-fractured systems.
- The fractures remain unconnected, even though we found evidences of mechanical deformation. Associated microcracks developed at weak structural points would remain saturated in brine during CO_2 injection due to the higher surface tension of the wetting phase.

Funding: We have received funding from the UK's Natural Environment Research Council (grant NE/R013535/1 GASRIP and grant NE/N016041/1 CHIMNEY), the European Union's Horizon 2020 research and innovation programme (grant No. 654462 STEMM-CCS), the project BIA2017-87066-R (MINECO/AEI/FEDER, UE), the Xunta de Galicia and the European Union (European Social Fund – ESF).

Acknowledgments: The experiment was conducted at the NOC Rock Physics Laboratory in Southampton. The authors thank Dr Laurence North for his support in the laboratory.

Author contributions: A.M.I. contribution roles include data curation, formal analysis, investigation, software, validation, visualization and writing – original draft; I.F.S. contribution roles include conceptualization, funding acquisition, methodology, project administration resources, supervision, visualization and writing – original draft; H.M.M.

contribution roles include conceptualization, formal analysis, software, validation and writing – review & editing; J.D.M. contribution roles include resources and writing – review & editing; P.M. contribution roles include formal analysis.

Declarations of Interest: The authors declare no conflict of interest. The funders had no role in the design of the study; in the collection, analyses, or interpretation of data; in the writing of the manuscript, and in the decision to publish the results.

Appendix A

Reactive transport modelling has been extensively applied to predict the behaviour of aquifers during and after CO_2 sequestration (e.g., Xu and Pruess (2001), Pruess and Müller (2009), André et al. (2010), Sung et al. (2014)).

The TOUGHREACT code has been previously used to simulate brine-CO_2 multi-flow processes in continuum idealized porous media (e.g. Pruess and Müller, 2009). We did not consider transport by molecular diffusion and performed an isothermal analysis. In addition, and although this program couples thermal, hydrologic and chemical (THC) processes, reactive transport was not considered since our siliciclastic sample is likely to remain chemically unaltered when exposed to brine and CO_2.

We developed a 2D axisymmetric radial model (20 mm thickness; 25 mm radius) of 500 grid elements. Cells between 0.5 and 2 mm wide were distributed in vertical layers of 1 mm, with a mesh refinement around the injection point and flow outlet to capture more precisely the processes occurring around them. An initial equilibrium simulation was performed to establish the initial pressure and temperature conditions for the BCFT simulation. In this equilibrium simulation, the grid blocks along the right, top, and bottom boundaries are kept constant at P = 100 bar; T = 19.6ºC; salinity = 3.5%; no CO_2 mass fraction. During the BCFT simulation, only the flow outlet element was kept at a constant pressure of 95 bar. The volume of the cell representing the injection point matches that of the diffusor pathway to better capture the injection velocities of the experiments. We used van Genuchten models (van Genuchten, 1980) for both water relative permeability and capillary pressure and Corey's model (Corey, 1954) for CO_2 relative permeability. Residual liquid and gas saturation values were obtained from experimental data. The simulation covers the six drainage stages and

1 the imbibition episode. Injection rates and partial flows varied according to the
2 experimental conditions. Table A.1 shows the parameters adopted in this model.

3 **Table A.1.** Modelling parameters

Rock property	*Symbol*	*Value*	*References*
Sample diameter (m)	$Ø$	0.05	
Sample thickness (m)	T	0.02	
Rock grain density (kg m^{-3})	ρ_s	2600	
Porosity	Φ	0.273	Experimental
Horizontal permeability (m^2)	K_H	$5.410x10^{-15}$	Experimental
Vertical permeability (m^2)	K_V	$5.410x10^{-16}$	Experimental
Rock thermal conductivity (W m^{-1} $ºC^{-1}$)	K	2	Eppelbaum et al. (Eppelbaum et al., 2014)
Rock specific heat (J kg^{-1} $ºC^{-1}$)	C	840	Eppelbaum et al. (Eppelbaum et al., 2014)
Pore compressibility (Pa^{-1})	c_p	8.69E-10	
Relative permeability parameters			
M		0.457	Pruess et al. (Pruess and Müller, 2009)
Residual liquid saturation	S_{wi}	0.1	Experimental
Liquid saturation		1.000	
Residual gas saturation	$S_{CO_2 i}$	0.07	Experimental
Capillary pressure parameters			
$m = 1 - 1/n$		0.457	Pruess et al. (Pruess and Müller, 2009)
Residual liquid saturation	S_{wi}	0.1	Experimental
$1/P_0$		5.1E-5	Pruess et al. (Pruess and Müller, 2009)
P_{max} (Pa)		1E7	
Liquid saturation		0.930	Experimental

4

5

6

References

Adler, A., Lionheart, W.R.B., 2006. Uses and abuses of EIDORS: an extensible software base for EIT. Physiol. Meas. 27, 25–42. https://doi.org/10.1088/0967-3334/27/5/S03

Akbarabadi, M., Piri, M., 2013. Relative permeability hysteresis and capillary trapping characteristics of supercritical CO_2/brine systems: An experimental study at reservoir conditions. Adv. Water Resour. 52, 190–206. https://doi.org/10.1016/j.advwatres.2012.06.014

Al-Khdheeawi, E.A., Vialle, S., Barifcani, A., Sarmadivaleh, M., Iglauer, S., 2017. Impact of reservoir wettability and heterogeneity on CO_2-plume migration and trapping capacity. Int. J. Greenh. Gas Control 58, 142–158. https://doi.org/10.1016/j.ijggc.2017.01.012

Al-Menhali, A., Krevor, S., 2014. Effective wettability measurements of CO_2-brine-sandstone system at different reservoir conditions. Energy Procedia 63, 5420–5426. https://doi.org/10.1016/j.egypro.2014.11.572

Alemu, B.L., Aker, E., Soldal, M., Johnsen, Ø., Aagaard, P., 2013. Effect of sub-core scale heterogeneities on acoustic and electrical properties of a reservoir rock: a CO_2 flooding experiment of brine saturated sandstone in a computed tomography scanner. Geophys. Prospect. 61, 235–250. https://doi.org/10.1111/j.1365-2478.2012.01061.x

Almenningen, S., Gauteplass, J., Fotland, P., Aastveit, G.L., Barth, T., Ersland, G., 2018. Visualization of hydrate formation during CO2 storage in water-saturated sandstone. Int. J. Greenh. Gas Control 79, 272–278. https://doi.org/10.1016/j.ijggc.2018.11.008

Amalokwu, K., Chapman, M., Best, A.I., Sothcott, J., Minshull, T.A., Li, X.-Y., 2015.

Experimental observation of water saturation effects on shear wave splitting in synthetic rock with fractures aligned at oblique angles. Geophys. J. Int. 200, 17–24. https://doi.org/10.1093/gji/ggu368

André, L., Azaroual, M., Menjoz, A., 2010. Numerical simulations of the thermal impact of supercritical CO_2 injection on chemical reactivity in a carbonate saline reservoir. Transp. Porous Media 82, 247–274. https://doi.org/10.1007/s11242-009-9474-2

Archie, G.E., 1942. The Electrical Resistivity Log as an Aid in Determining Some Reservoir Characteristics. Trans. AIME 146, 54–62. https://doi.org/10.2118/942054-G

Bachu, S., 2015. Review of CO_2 storage efficiency in deep saline aquifers. Int. J. Greenh. Gas Control 40, 188–202. https://doi.org/10.1016/j.ijggc.2015.01.007

Bachu, S., 2013. Drainage and imbibition CO_2/brine relative permeability curves at in situ conditions for sandstone formations in western Canada. Energy Procedia 37, 4428–4436. https://doi.org/10.1016/j.egypro.2013.07.001

Bachu, S., Bennion, B., 2009. Dependence of CO_2 -brine interfacial tension on aquifer pressure, temperature and water salinity. Energy Procedia 1, 3157–3164. https://doi.org/10.1016/j.egypro.2009.02.098

Bachu, S., Bennion, B., 2008. Effects of in-situ conditions on relative permeability characteristics of CO_2-brine systems. Environ. Geol. 54, 1707–1722. https://doi.org/10.1007/s00254-007-0946-9

Batzle, M., Wang, Z., 1992. Seismic properties of pore fluids. Geophysics 57, 1396–1408. https://doi.org/10.1190/1.1443207

Baumann, G., Henninges, J., De Lucia, M., 2014. Monitoring of saturation changes and salt precipitation during CO_2 injection using pulsed neutron-gamma logging

at the Ketzin pilot site. Int. J. Greenh. Gas Control 28, 134–146. https://doi.org/10.1016/j.ijggc.2014.06.023

Bennion, B., Bachu, S., 2006. The impact of interfacial tension and pore size distribution/capillary pressure character on CO_2 relative permeability at reservoir conditions in CO_2-brine systems, in: 2006 SPE/DOE Symposium on Improved Oil Recovery. Tulsa, Oklahoma, U.S.A., 22–26 April. https://doi.org/10.2523/99325-MS

Berg, S., Oedai, S., Ott, H., 2013. Displacement and mass transfer between saturated and unsaturated CO_2-brine systems in sandstone. Int. J. Greenh. Gas Control 12, 478–492. https://doi.org/10.1016/j.ijggc.2011.04.005

Bond, C.E., Wightman, R., Ringrose, P.S., 2013. The influence of fracture anisotropy on CO_2 flow. Geophys. Res. Lett. 40, 1284–1289. https://doi.org/10.1002/grl.50313

Broseta, D., Tonnet, N., Shah, V., 2012. Are rocks still water-wet in the presence of dense CO_2 or H_2S? Geofluids 12, 280–294. https://doi.org/10.1111/j.1468-8123.2012.00369.x

Cai, J., Wei, W., Hu, X., Wood, D.A., 2017. Electrical conductivity models in saturated porous media: A review. Earth-Science Rev. 171, 419–433. https://doi.org/10.1016/j.earscirev.2017.06.013

Canal, J., Delgado, J., Falcón, I., Yang, Q., Juncosa, R., Barrientos, V., 2013. Injection of CO_2-saturated water through a siliceous sandstone plug from the Hontomin test site (Spain): Experiment and modeling. Environ. Sci. Technol. 47, 159–167. https://doi.org/10.1021/es3012222

Carrigan, C.R., Yang, X., LaBrecque, D.J., Larsen, D., Freeman, D., Ramirez, A.L., Daily, W., Aines, R., Newmark, R., Friedmann, J., Hovorka, S., 2013. Electrical

resistance tomographic monitoring of CO_2 movement in deep geologic reservoirs. Int. J. Greenh. Gas Control 18, 401–408. https://doi.org/10.1016/j.ijggc.2013.04.016

Castillo, S.C., Skjaeveland, S., Fjelde, I., 2011. Water and surfactant flooding at different wettability conditions. Mycotoxin Res. 6, 77. https://doi.org/10.1007/BF03192151

Chiquet, P., Broseta, D., Thibeau, S., 2007. Wettability alteration of caprock minerals by carbon dioxide. Geofluids 7, 112–122. https://doi.org/10.1111/j.1468-8123.2007.00168.x

Corey, A.T., 1954. The interrelation between gas and oil relative permeabilities. Prod. Mon. 19, 38–41.

Dandekar, A.Y., 2013. Petroleum Reservoir Rock and Fluid Properties, Second Edition. CRC Press. https://doi.org/10.1201/b15255

Diomampo, G.P., 2001. Relative permeability through fractures. Stanford University, Stanford, USA. https://doi.org/10.2172/896520

Duan, Z., Sun, R., Zhu, C., Chou, I.M., 2006. An improved model for the calculation of CO2 solubility in aqueous solutions containing Na+, K^+, Ca^{2+}, Mg^{2+}, Cl^-, and SO_4^{2-}. Mar. Chem. 98, 131–139. https://doi.org/10.1016/j.marchem.2005.09.001

Dullien, F.A.L., 1992. Porous media: fluid transport and pore structure. Second edition. Academic Press Inc. https://doi.org/doi.org/10.1016/B978-0-12-223651-8.50001-8

El-Maghraby, R.M., Pentland, C.H., Iglauer, S., Blunt, M.J., 2012. A fast method to equilibrate carbon dioxide with brine at high pressure and elevated temperature including solubility measurements. J. Supercrit. Fluids 62, 55–59. https://doi.org/10.1016/j.supflu.2011.11.002

Eppelbaum, L., Kutasov, I., Pilchin, A., 2014. Thermal properties of rocks and density of fluids, in: Applied Geothermics. Lecture Notes in Earth System Sciences. Springer, Berlin, Heidelberg, pp. 99–149. https://doi.org/10.1007/978-3-642-34023-9_2

Falcon-Suarez, I., Marín-Moreno, H., Browning, F., Lichtschlag, A., Robert, K., North, L.J., Best, A.I., 2017. Experimental assessment of pore fluid distribution and geomechanical changes in saline sandstone reservoirs during and after CO_2 injection. Int. J. Greenh. Gas Control 63, 356–369. https://doi.org/10.1016/j.ijggc.2017.06.019

Falcon-Suarez, I., North, L., Amalokwu, K., Best, A., 2016. Integrated geophysical and hydromechanical assessment for CO_2 storage: shallow low permeable reservoir sandstones. Geophys. Prospect. 64, 828–847. https://doi.org/10.1111/1365-2478.12396

Falcon-Suarez, I., Papageorgiou, G., Chadwick, A., North, L., Best, A.I., Chapman, M., 2018. CO_2-brine flow-through on an Utsira Sand core sample: Experimental and modelling. Implications for the Sleipner storage field. Int. J. Greenh. Gas Control 68, 236–246. https://doi.org/10.1016/j.ijggc.2017.11.019

Falcon-Suarez, I.H., Amalokwu, K., Delgado-Martin, J., Callow, B., Robert, K., North, L., Sahoo, S.K., Best, A.I., 2019. Comparison of stress-dependent geophysical, hydraulic and mechanical properties of synthetic and natural sandstones for reservoir characterization and monitoring studies. Geophys. Prospect. 67, 784–803. https://doi.org/10.1111/1365-2478.12699

Farajzadeh, R., Zitha, P.L.J., Bruining, J., 2009. Enhanced mass transfer of CO_2 into water: Experiment and modeling. Ind. Eng. Chem. Res. 48, 6423–6431. https://doi.org/10.1021/ie801521u

Fjaer, E., Holt, R.M., Horsrud, P., Raaen, A.M., Risnes, R., 2008. Petroleum related rock mechanics. 2nd edition. Elsevier. https://doi.org/10.1016/0148-9062(93)92632-Z

Fortin, J., Guéguen, Y., Schubnel, A., 2007. Effects of pore collapse and grain crushing on ultrasonic velocities and V_p/V_s. J. Geophys. Res. 112, B08207. https://doi.org/10.1029/2005JB004005

Fourar, M., Bories, S., 1995. Experimental study of air-water two-phase flow through a fracture (narrow channel). Int. J. Multiph. Flow 21, 621–637. https://doi.org/10.1016/0301-9322(95)00005-I

Grude, S., Landrø, M., Dvorkin, J., 2014. Pressure effects caused by CO_2 injection in the Tubåen Fm., the Snøhvit field. Int. J. Greenh. Gas Control 27, 178–187. https://doi.org/10.1016/j.ijggc.2014.05.013

Hangx, S., Bakker, E., Bertier, P., Nover, G., Busch, A., 2015. Chemical–mechanical coupling observed for depleted oil reservoirs subjected to long-term CO_2 - exposure – A case study of the Werkendam natural CO_2 analogue field. Earth Planet. Sci. Lett. 428, 230–242. https://doi.org/10.1016/j.epsl.2015.07.044

Huo, D., Benson, S.M., 2016. Experimental investigation of stress-dependency of relative permeability in rock fractures. Transp. Porous Media 113, 567–590. https://doi.org/10.1007/s11242-016-0713-z

Iding, M., Ringrose, P., 2010. Evaluating the impact of fractures on the performance of the In Salah CO_2 storage site. Int. J. Greenh. Gas Control 4, 242–248. https://doi.org/10.1016/j.ijggc.2009.10.016

IPCC, 2005. Carbon dioxide capture and storage. Special report. Cambridge University Press.

Jackson, S.J., Agada, S., Reynolds, C.A., Krevor, S., 2018. Characterizing Drainage

Multiphase Flow in Heterogeneous Sandstones. Water Resour. Res. 54, 3139–3161. https://doi.org/10.1029/2017WR022282

Kim, M., Sell, A., Sinton, D., 2013. Aquifer-on-a-Chip: understanding pore-scale salt precipitation dynamics during CO_2 sequestration. Lab Chip 13, 2421–2662. https://doi.org/10.1039/c3lc00031a

Krevor, S., Blunt, M.J., Benson, S.M., Pentland, C.H., Reynolds, C., Al-Menhali, A., Niu, B., 2015. Capillary trapping for geologic carbon dioxide storage – From pore scale physics to field scale implications. Int. J. Greenh. Gas Control 40, 221–237. https://doi.org/10.1016/j.ijggc.2015.04.006

Krevor, S.C.M., Pini, R., Zuo, L., Benson, S.M., 2012. Relative permeability and trapping of CO_2 and water in sandstone rocks at reservoir conditions. Water Resour. Res. 48, W02532. https://doi.org/10.1029/2011WR010859

Lee, J., Choi, S.-U., Cho, W., 1999. A comparative study of dual-porosity model and discrete fracture network model. KSCE J. Civ. Eng. 3, 171–180. https://doi.org/10.1007/BF02829057

Leverett, M.C., 1941. Capillary Behavior in Porous Solids. Trans. AIME 142, 152–169. https://doi.org/10.2118/941152-G

Li, K., 2008. A new method for calculating two-phase relative permeability from resistivity data in porous media. Transp. Porous Media 74, 21–33. https://doi.org/10.1007/s11242-007-9178-4

Li, K., Horne, R.N., 2006. Comparison of methods to calculate relative permeability from capillary pressure in consolidated water-wet porous media. Water Resour. Res. 42, W06405. https://doi.org/10.1029/2005WR004482

March, R., Doster, F., Geiger, S., 2018. Assessment of CO_2 storage potential in naturally fractured reservoirs with dual-porosity models. Water Resour. Res. 54,

1650–1668. https://doi.org/10.1002/2017WR022159

Mavko, G., Mukerji, T., Dvorkin, J., 2009. The rock physics handbook. Tools for seismic analysis of porous media. Second edition. Cambridge University Press. https://doi.org/10.1017/CBO9780511626753

Michael, K., Golab, A., Shulakova, V., Ennis-King, J., Allinson, G., Sharma, S., Aiken, T., 2010. Geological storage of CO_2 in saline aquifers—A review of the experience from existing storage operations. Int. J. Greenh. Gas Control 4, 659–667. https://doi.org/10.1016/j.ijggc.2009.12.011

Müller, N., 2011. Supercritical CO_2-brine relative permeability experiments in reservoir rocks—Literature review and recommendations. Transp. Porous Media 87, 367–383. https://doi.org/10.1007/s11242-010-9689-2

Nakatsuka, Y., Xue, Z., Garcia, H., Matsuoka, T., 2010. Experimental study on CO_2 monitoring and quantification of stored CO_2 in saline formations using resistivity measurements. Int. J. Greenh. Gas Control 4, 209–216. https://doi.org/10.1016/j.ijggc.2010.01.001

Nooraiepour, M., Bohloli, B., Park, J., Sauvin, G., Skurtveit, E., Mondol, N.H., 2018. Effect of brine-CO_2 fracture flow on velocity and electrical resistivity of naturally fractured tight sandstones. Geophysics 83, WA37–WA48. https://doi.org/10.1190/geo2017-0077.1

Noriaki, W., Keisuke, S., Takuya, I., Yutaka, O., Tetsuya, T., Masahiko, Y., Noriyoshi, T., 2015. New v-type relative permeability curves for two-phase flows through subsurface fractures. Water Resour. Res. 51, 2807–2824. https://doi.org/10.1002/2014WR016515

North, L., Best, A.I., Sothcott, J., MacGregor, L., 2013. Laboratory determination of the full electrical resistivity tensor of heterogeneous carbonate rocks at elevated

pressures. Geophys. Prospect. 61, 458–470. https://doi.org/10.1111/j.1365-2478.2012.01113.x

Oostrom, M., White, M.D., Porse, S.L., Krevor, S.C.M., Mathias, S.A., 2016. Comparison of relative permeability–saturation–capillary pressure models for simulation of reservoir CO_2 injection. Int. J. Greenh. Gas Control 45, 70–85. https://doi.org/https://doi.org/10.1016/j.ijggc.2015.12.013

Papageorgiou, G., Falcon-Suarez, I., Chapman, M., Best, A., 2018. Pressure-varying CO_2 distribution affects the ultrasonic velocities of synthetic sandstones. Int. J. Greenh. Gas Control 74, 1–8. https://doi.org/10.1016/j.ijggc.2018.03.022

Park, J., Fawad, M., Viken, I., Aker, E., Bjørnarå, T.I., 2013. CSEM sensitivity study for Sleipner CO_2-injection monitoring. Energy Procedia 37, 4199–4206. https://doi.org/10.1016/j.egypro.2013.06.322

Pollard, D.D., Aydin, A., 1988. Progress in understanding jointing over the past century, in: General Society of America Bulletin. pp. 1181–1204. https://doi.org/10.1130/SPE253-p313

Pruess, K., 2005. ECO2N: A TOUGH2 fluid property module for mixtures of water, NaCl,and CO_2. Berkeley, CA. https://doi.org/10.2172/877331

Pruess, K., Müller, N., 2009. Formation dry-out from CO_2 injection into saline aquifers: 1. Effects of solids precipitation and their mitigation. Water Resour. Res. 45, 1–11. https://doi.org/10.1029/2008WR007101

Purcell, W.R., 1949. Capillary pressures - Their measurement using mercury and the calculation of permeability therefrom. J. Pet. Technol. 1, 39–48. https://doi.org/10.2118/949039-G

Reynolds, C., Krevor, S., 2017. Capillary limited flow behavior of CO_2 in target reservoirs in the UK. Energy Procedia 114, 4518–4523.

https://doi.org/10.1016/j.egypro.2017.03.1568

Reynolds, C.A., 2016. Two-phase flow behaviour and relative permeability between CO_2 and brine in sandstones at the pore and core scales. Imperial College London.

Reynolds, C.A., Blunt, M.J., Krevor, S., 2018. Multiphase flow characteristics of heterogeneous rocks from CO_2 storage reservoirs in the United Kingdom. Water Resour. Res. 54, 729–745. https://doi.org/10.1002/2017WR021651

Shi, J.-Q., Xue, Z., Durucan, S., 2011. Supercritical CO_2 core flooding and imbibition in Berea sandstone — CT imaging and numerical simulation. Energy Procedia 4, 5001–5008. https://doi.org/10.1016/j.egypro.2011.02.471

Shi, J.-Q., Xue, Z., Durucan, S., 2007. Seismic monitoring and modelling of supercritical CO_2 injection into a water-saturated sandstone: Interpretation of P-wave velocity data. Int. J. Greenh. Gas Control 1, 473–480. https://doi.org/10.1016/S1750-5836(07)00013-8

Stack, A.G., Fernandez-Martinez, A., Allard, L.F., Bañuelos, J.L., Rother, G., Anovitz, L.M., Cole, D.R., Waychunas, G.A., 2014. Pore-size-dependent calcium carbonate precipitation controlled by surface chemistry. Environ. Sci. Technol. 48, 6177–6183. https://doi.org/10.1021/es405574a

Sung, R.-T., Li, M.-H., Dong, J.-J., Lin, A.T.-S., Hsu, S.-K., Wang, C.-Y., Yang, C.-N., 2014. Numerical assessment of CO_2 geological sequestration in sloping and layered heterogeneous formations: A case study from Taiwan. Int. J. Greenh. Gas Control 20, 168–179. https://doi.org/10.1016/j.ijggc.2013.11.003

Tillotson, P., Sothcott, J., Best, A.I., Chapman, M., Li, X.-Y., 2012. Experimental verification of the fracture density and shear-wave splitting relationship using synthetic silica cemented sandstones with a controlled fracture geometry.

Geophys. Prospect. 60, 516–525. https://doi.org/10.1111/j.1365-2478.2011.01021.x

Tsuji, T., Jiang, F., Christensen, K.T., 2016. Characterization of immiscible fluid displacement processes with various capillary numbers and viscosity ratios in 3D natural sandstone. Adv. Water Resour. 95, 3–15. https://doi.org/10.1016/j.advwatres.2016.03.005

van Genuchten, M.T., 1980. A closed-form equation for predicting the hydraulic conductivity of unsaturated soils. Soil Sci. Soc. Am. J. 44, 892–898. https://doi.org/10.2136/sssaj1980.03615995004400050002x

Wang, S., Tokunaga, T.K., 2015. Capillary Pressure–Saturation Relations for Supercritical CO_2 and Brine in Limestone/Dolomite Sands: Implications for Geologic Carbon Sequestration in Carbonate Reservoirs. Environ. Sci. Technol. 49, 7208–7217. https://doi.org/10.1021/acs.est.5b00826

Wang, Z., Gelius, L.-J., Kong, F.-N., 2009. Simultaneous core sample measurements of elastic properties and resistivity at reservoir conditions employing a modified triaxial cell - a feasibility study. Geophys. Prospect. 57, 1009–1026. https://doi.org/10.1111/j.1365-2478.2009.00792.x

Xu, T., Pruess, K., 2001. Modeling multiphase non-isothermal fluid flow and reactive geochemical transport in variably saturated fractured rocks: 1. Methodology. Am. J. Sci. 301, 16–33. https://doi.org/10.2475/ajs.301.1.16

Xu, T., Sonnenthal, E., Spycher, N., Pruess, K., 2017. TOUGHREACT V3.32 Reference manual: A parallel simulation program for non-isothermal multiphase geochemical reactive transport, Report LBNL-Draft. Berkeley, California. https://doi.org/10.1016/j.cageo.2005.06.014

Xu, T., Sonnenthal, E., Spycher, N., Pruess, K., 2004. TOUGHREACT user's guide:

A simulation program for non-isothermal multiphase reactive geochemical transport in variable saturated geologic media. Earth Sciences Division, Lawrence Berkeley National Laboratory, Berkeley, CA. https://doi.org/10.2172/834237

Yoshida, N., Levine, J.S., Stauffer, P.H., 2016. Investigation of uncertainty in CO_2 reservoir models: A sensitivity analysis of relative permeability parameter values. Int. J. Greenh. Gas Control 49, 161–178. https://doi.org/10.1016/j.ijggc.2016.03.008

Zhu, Q., Zhou, Q., Li, X., 2016. Numerical simulation of displacement characteristics of CO_2 injected in pore-scale porous media. J. Rock Mech. Geotech. Eng. 8, 87–92. https://doi.org/10.1016/j.jrmge.2015.08.004